

RESEARCH ARTICLE

10.1002/2016JA023352

Special Section:

Geospace system responses to the St. Patrick's Day storms in 2013 and 2015

Key Points:

- Three equatorward TIDs of the main phase through multiple methods
- The evolution of the global negative storm in the recovery phase
- Inverse hemispheric asymmetry in intensity and structure

Supporting Information:

- Supporting Information S1

Correspondence to:

Y. Yao,
ybyao@whu.edu.cn

Citation:

Yao, Y., L. Liu, J. Kong, and C. Zhai (2016), Analysis of the global ionospheric disturbances of the March 2015 great storm, *J. Geophys. Res. Space Physics*, 121, 12,157–12,170, doi:10.1002/2016JA023352.

Received 17 AUG 2016

Accepted 20 NOV 2016

Accepted article online 22 NOV 2016

Published online 22 DEC 2016

©2016. American Geophysical Union.
All Rights Reserved.

Analysis of the global ionospheric disturbances of the March 2015 great storm

Yibin Yao^{1,2,3} , Lei Liu¹ , Jian Kong⁴, and Changzhi Zhai¹ 

¹School of Geodesy and Geomatics, Wuhan University, Wuhan, China, ²Key Laboratory of Geospace Environment and Geodesy, Ministry of Education, Wuhan University, Wuhan, China, ³Collaborative Innovation Center for Geospatial Technology, Wuhan, China, ⁴Chinese Antarctic Center of Surveying and Mapping, Wuhan University, Wuhan, China

Abstract The global ionospheric storm in March 2015 was investigated by using data from over 3000 GPS stations worldwide. In this study, total electron content (TEC), rate of TEC (ROT), and ROT's standard deviation rate of the TEC index, as well as the second-order difference operator TECT, were considered as main characteristic methods to distinguish ionospheric disturbances. The results show that (1) based on the multiple methods above, we all observed that for the first time, there were three equatorward traveling ionospheric disturbances (TIDs) in the main phase of this storm. In North America, the disturbance zone expanded to ~40°N; the disturbance periods and AE peak stages were roughly synchronous. We suggest that these three TIDs were induced by the propagation of atmospheric gravity waves to low latitudes under the action of AE. (2) The most intense positive storm occurred over South America and the South Atlantic (over 300% enhancement; 00:00–05:00 UT on 18 March), whereas a negative storm was observed in the corresponding region of the Northern Hemisphere. Such inverse hemispheric asymmetry in intensity and structure can be explained by the variations of the thermospheric composition, the IMF B_y component, and the geomagnetic intensity. (3) On 18 March, a negative storm dominated globally (except at certain low latitudes), and tended to propagate equatorward and decay with time, which could be largely attributed to the storm circulation theory. And the evolution of the negative storm was further characterized by the f_oF_2 variations of ionosondes.

1. Introduction

Due to the influence of coronal mass ejections (CMEs) or coronal hole high-speed streams, the interplanetary magnetic field (IMF) B_z component turns southward and intensifies. As this occurs, the solar wind energy enters the magnetosphere-ionosphere-thermosphere system suddenly by setting up an interconnection between the southward IMF and the Earth's magnetic field lines. Consequently, the geomagnetic space environment is strongly disturbed, and a global ionospheric storm occurred [Pi et al., 1997; Aarons, 1997; Farrugia et al., 2006; Kamide and Kusano, 2015]. Such severe storms can disrupt radio communications and degrade satellite navigation and positioning performance [Skone and Yousuf, 2007; Astafyeva et al., 2014], as well as cause breakdowns in high-voltage power transmission networks [Kappenman, 1996].

During auroral substorms, energetic particles precipitate in the auroral or subauroral regions, and heat the upper atmosphere in the form of Joule heating and Lorentz forces. As a result, large-scale traveling ionospheric disturbances (LSTIDs) are most likely to recognize as ionospheric manifestations of atmospheric gravity waves (AGWs) that are generated by the energy input of the auroral ionosphere. Generally, the propagation of LSTIDs is believed to have horizontal phase velocities between 300 and 1000 m/s and cycle periods in the range of 30–180 min [Hunsucker, 1982; Tsugawa et al., 2003, 2007; Ding et al., 2007]. Also, pressure gradients caused by the intense Joule heating in the high-latitude ionosphere allow equatorward neutral winds to transmit to mid-low latitudes and lead to changes in the O/N₂ ratio of the ionosphere and thermosphere [Fuller-Rowell et al., 1994; Fang et al., 2012]. This process, in turn, is one dominant mechanism of both increases (positive storm effects) and decreases (negative storm effects) in the electron plasma densities and total electron content (TEC).

However, neutral composition changes are not the sole driver of the ionosphere storm effects. For example, the prompt penetration of high-latitude magnetosphere electric fields, the propagation of disturbance dynamo electric fields to mid-low latitudes, and the enhancement of plasma convection, as well as combinations of these above factors, may also cause ionospheric storms of varying degrees [Rishbeth and Setty, 1961;

Fuller-Rowell et al., 1994; Zhao et al., 2009; Fang et al., 2012; Tsurutani et al., 2004; Mannucci et al., 2008; Blanc and Richmond, 1980; Maruyama et al., 2005; Lemaire and Gringauz, 1998; Schunk and Nagy, 2000; Zhu et al., 2007].

Some scholars have proposed that the prompt penetration of high-latitude magnetospheric electric fields toward low latitudes can produce strong eastward dayside (dawn-to-dusk) electric field disturbances at mid-low latitudes, which elevate ionospheric height, increase F region TEC, and further enhance the development of the dayside superfountain effect; meanwhile, negative disturbances propagate from high latitudes to low latitudes [Tsurutani et al., 2004; Huang et al., 2005; Kikuchi et al., 2008; Mannucci et al., 2008]. Others have suggested that disturbance dynamo electric fields generated by high-latitude energy precipitation can influence ionospheric disturbances of the mid-low latitudes and that the equatorial expansion of this disturbance has a certain time delay [Blanc and Richmond, 1980; Scherliess and Fejer, 1997; Buonsanto, 1999; Maruyama et al., 2005]. Additionally, it has been argued that the combination of high-speed solar wind and strong southward IMF B_z , which result in the enhancement of large-scale plasma convection and increases of the current, can further change the plasma drift and the ionization of gas, and ultimately affect the ionospheric structure [Lemaire and Gringauz, 1998; Schunk and Nagy, 2000]. Overall, the ionosphere shows complex disturbance characteristics driven by these interacting physical processes.

The March 2015 storm, triggered by CMEs, was the strongest storm in solar cycle 24 so far, and some studies on the ionosphere response of this storm have been made [e.g., Cherniak et al., 2015; Astafyeva et al., 2015; Liu et al., 2016a, 2016b; Zhong et al., 2016; Nayak et al., 2016]. Liu et al. [2016a] studied the ionospheric storm-enhanced density (SED) in the main phase and found that there was a SED in TEC but not in N_mF_2 . Zhong et al. [2016] reported that there was a long-duration topside TEC depletion in the recovery phase. Nayak et al. [2016] studied the ionosphere effects of this storm at the low latitudes and midlatitudes and found that the coexistence of both positive and negative ionospheric storm phases was presented in the American sector. In this paper, based on the data from more than 3000 GPS stations worldwide, we mainly focus on the comprehensive ionospheric response on a global scale in both the main and recovery phase, which has not been studied enough to date for this storm. Also, possible physical mechanisms behind this ionospheric storm are discussed.

2. The St. Patrick's Day Geomagnetic Storm

The strongest storm of solar cycle 24 thus far commenced on 17 March (St. Patrick's Day), 2015, lasting for over 24 h and causing a dramatic response in the magnetosphere-ionosphere-thermosphere system. This unexpected storm resulted from the interaction of a pair of successive CMEs on 15 March; the plasma cloud plus the compression of a high-speed solar wind hit the geomagnetic field directly, thus causing substantial plasma precipitation and inducing auroral substorm activities [Cherniak et al., 2015; Astafyeva et al., 2015; Liu et al., 2016a, 2016b].

Variations of the interplanetary and geomagnetic parameters during 15–20 March 2015 are presented in Figure 1. The storm sudden commencement was registered at ~04:45 UT on 17 March. The solar wind speed and pressure measured by the Advanced Composition Explorer increased, respectively, from 400 km/s to over 500 km/s, and from approximately 300 nPa to over 500 nPa; meanwhile, $SYM-H$ increased suddenly to 53 nT from a stationary state, the K_p index reached 5, and the IMF B_z component approached ~25 nT, pointing north. Afterward, the development of the storm can be divided into three typical stages: the initial phase (~04:45–07:30 UT), the main phase (~07:30–22:45 UT), and the recovery phase (after 22:45 UT).

In the main phase, the solar wind speed (~600 km/s) and pressure (13–25 nPa) increased significantly relative to the quiet days, with a K_p index between 5 and 8, which indicated that the storm reached a moderate to active level. AE reached its first peak value of 981 nT at ~08:50 UT, and another peak appeared at 13:55 UT; B_z varied drastically from north to south between these two AE peak values. AE reached its maximum peak for a third time during 17:00–24:00 UT. Each AE peak stage may be associated with large amounts of O^+ being injected into the inner magnetosphere. Figure 1 shows that the three peak stages of AE were roughly synchronous with the three minimum phases of $SYM-H$, which were approximately -99 nT (09:35 UT), -174 nT (17:25 UT), and -233 nT (22:45 UT), respectively. Visibly, the $SYM-H$ of the main phase decayed mainly through not one but three stages. The first phase of $SYM-H$ decay may have been driven by the arrival

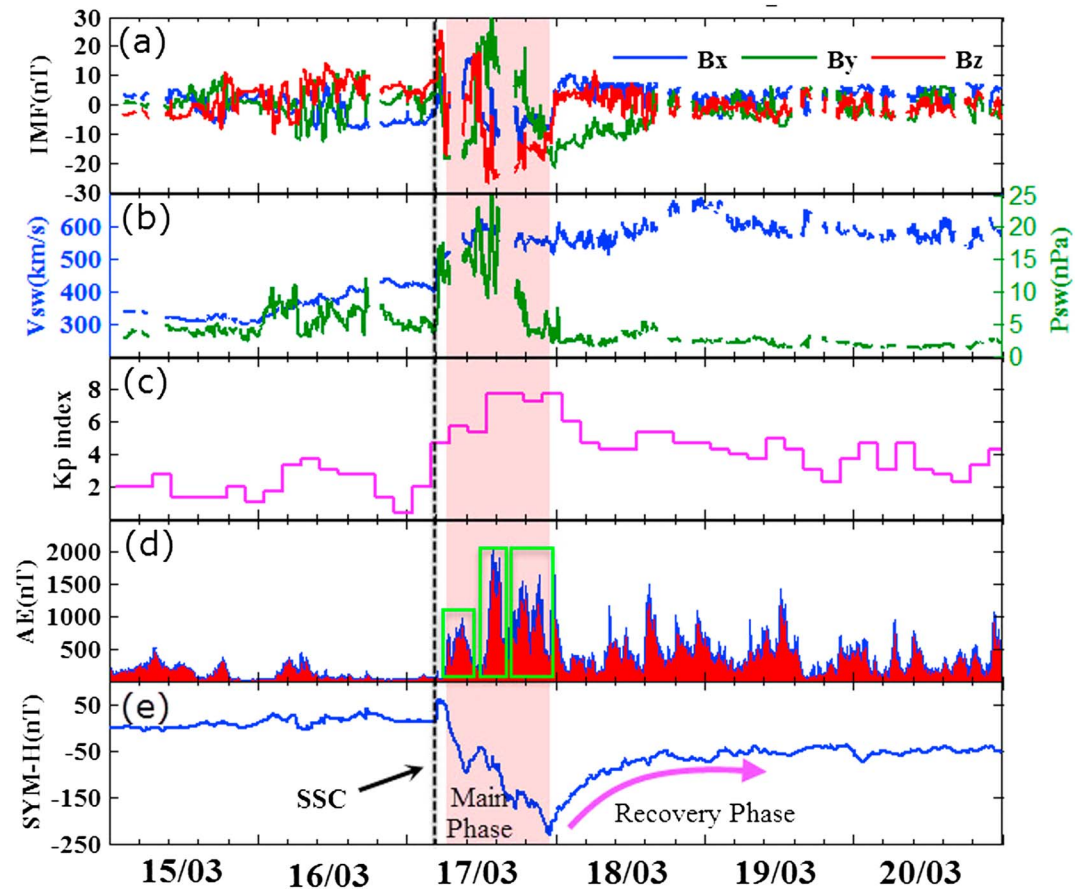


Figure 1. Variations of geomagnetic conditions during 15–20 March 2015: (a) Interplanetary magnetic field (IMF) B_x , B_y , and B_z components; (b) velocity and dynamic pressure of the solar wind; (c) K_p index; (d) auroral electrojet (AE) index; and (e) SYM-H index.

of the first southward IMF B_z . The later two-phase decay, which was characterized by different time scales, was mostly likely to be the result of the abrupt enhancement of the polar ring current [Kamide *et al.*, 1998; Kozyra *et al.*, 2002]. In the recovery phase, the IMF B_y remained directed southward; the solar wind and geomagnetic indices remained higher than those of quiet days.

3. Data and Methodology

For this study, the dual-frequency observations from over 3000 ground-based GPS stations, provided by the Scripps Orbit and Permanent Array Center (SOPAC), the European Reference Frame Permanent Network (EUREF), the Canadian Active Control System (CACS), the Crustal Movement Observation Network of China (CMONOC), and the Geoscience Australia, are used to investigate this storm (see Figure 2). Meanwhile, O/N_2 ratio maps provided by Thermosphere Ionosphere Mesosphere Energetics and Dynamics (TIMED)/Global Ultraviolet Imager (GUVI), ionosondes f_oF_2 data in China, and vertical TEC of global ionosphere maps (GIMs) are also used for this study.

Based on the inverse relationship between the ionospheric delay of the GPS signal and the square of the signal frequency, the line-of-sight ionospheric TEC (in units of TECU, $1 \text{ TECU} = 10^{16} \text{ el/m}^2$) along the propagation path from satellite to receiver can be determined. Without considering the absolute TEC value, the relative TEC_ϕ (with an accuracy better than 0.01 TECU) can be evaluated with high precision from the geometric-free combination of the carrier phase measurements [Saito *et al.*, 1998]:

$$\text{TEC}_\phi = \frac{f_1^2 f_2^2}{40.3(f_2^2 - f_1^2)} (\phi_1 - \phi_2) \quad (1)$$

where f_1 and f_2 are the frequencies of carrier phases ϕ_1 and ϕ_2 , respectively.

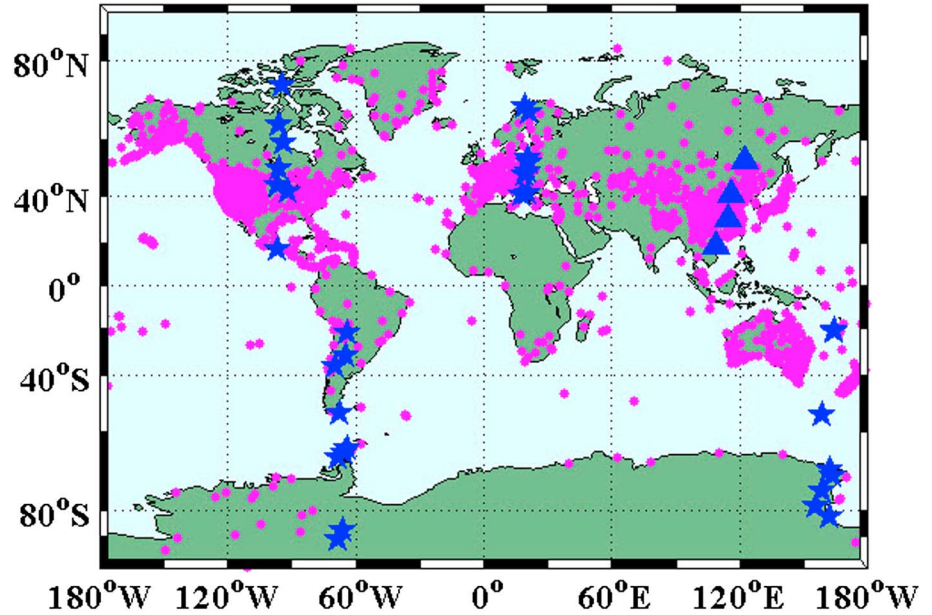


Figure 2. Instruments and data used in this study. GPS receivers across the globe are indicated by magenta circles, GPS receivers in selected meridional chains are indicated by blue stars, and ionosondes in China are indicated by blue triangles.

After extracting TEC_{ϕ} , the rate of TEC (ROT, in units of TECU/min) is defined to detect irregular phase fluctuations by measuring the time rate of TEC_{ϕ} . To identify and statistically present smaller-scale irregularities, we define the rate of the TEC index (ROTI) based on the standard deviation of the ROT [Pi et al., 1997]:

$$\begin{cases} ROT = \frac{TEC_{\phi}(t + dt) - TEC_{\phi}(t)}{dt} \\ ROTI = \sqrt{\langle ROT^2 \rangle - \langle ROT \rangle^2} \end{cases} \quad (2)$$

where dt is typically sampled at 30 s, the cutoff elevation angle is 20° when the ROT is computed for all visible GPS satellites, and the ROT is detrended and used to obtain the ROTI with a sliding window for each 10 min time interval.

Another indicator the second-order difference operator TECT is also used to extract the ionospheric disturbance of the satellite arc. The principle of TECT is to predict the current epoch's normal ionospheric changes based on the prior two epochs' TEC variations. After the normal ionospheric changes of the current epoch are removed, the abnormal changes can be detected more precisely. As shown in formula (3), there is a set of TEC_{ϕ} time sequences from a pair of receiver and satellite arcs:

$$TEC_{\phi,1}, \dots, TEC_{\phi,i-1}, TEC_{\phi,i}, TEC_{\phi,i+1}, \dots, TEC_{\phi,n} \quad (3)$$

The ionospheric disturbance at the i th epoch can be determined as the test value given by formula (4):

$$\begin{aligned} TEC_TEST = TECT = TEC_{\phi,i} - (TEC_{\phi,i-1} + TECV_{EST}) \\ TECV_{EST} = TEC_{\phi,i-1} - TEC_{\phi,i-2} = \frac{f_1^2 f_2^2}{40.3(f_2^2 - f_1^2)} [\Delta\phi_1(i-1) - \Delta\phi_2(i-1)] \text{ (see formula (1))} \\ \text{Then} \\ TECT = \frac{f_1^2 f_2^2}{40.3(f_2^2 - f_1^2)} [(\Delta\phi_1(i) - \Delta\phi_2(i)) - (\Delta\phi_1(i-1) - \Delta\phi_2(i-1))] \\ \Delta\phi_j(i) = \phi_j(i) - \phi_j(i-1), j = 1, 2 \end{aligned} \quad (4)$$

where TECT is the second-order difference operator calculated by carrier observations. The above method can easily confirm whether irregular disturbances occurred.

4. Results

4.1. Global Overview of the Storm in the Spatial and Temporal Domains

To have a spatial overview of the global vertical TEC (VTEC) behavior during the storm, we obtain absolute VTEC maps (see Figure S1 in the supporting-information) calculated from global GPS stations [Schaer, 1999; Rideout and Coster, 2006], then the differential VTEC percentage maps (see Figure S2) between the 5 day mean value $VTEC_{ref}$ (11–15 March) and the daily value $VTEC_{daily}$ (16–19 March) can be calculated by formula (5):

$$\Delta VTEC(\%) = \frac{VTEC_{daily} - VTEC_{ref}}{VTEC_{ref}} \times 100 \quad (5)$$

As shown in Figure S2, because of the quiet geomagnetic condition of 16 March, the daily $\Delta VTEC(\%)$ was controlled within $\pm 30\%$. This small variation of VTEC (20–30%) is regarded as the normal diurnal variation of the ionosphere [Rishbeth and Mendillo, 2001]. Therefore, in the subsequent discussion, we propose that the storm was not responsible for daily VTEC variations within 30%. However, it is apparent that a global ionospheric disturbance with a large amplitude occurred on 17–18 March and that the intensity of the storm declined on 19 March.

The first VTEC enhancement of the storm began to occur at high latitudes of the Northern Hemisphere (NH) at 05:00 UT on 17 March; the maximum increment was approximately 50% from the mean VTEC. In the following 7 h, V_{sw} and P_{sw} were maintained at high levels ($V_{sw} \approx 600$ km/s, $P_{sw} \approx 20$ nPa); the positive storm at high latitudes gradually strengthened (the maximum increment was over 150%). From 12:00 UT to 15:00 UT, a weak negative storm (decrement of approximately -50% to -80%) dominated in the high latitudes of the Southern Hemisphere (SH), while the range and amplitude of the positive storm in the NH declined. In addition, at this time, the *AE* index was in the low level, which also corresponded to the first short recovery phase of the *SYM-H*, and indicated a decrease of the auroral activity. At around 16:00 UT, a TEC SED structure began to emerge over the east of Canada (see Figure S1). In the next 8 h, this SED structure gradually drifted westward, and TEC gradients associated with SED were apparent over the North American continent. Because of the large TEC gradients, small-scale irregularities were thought to form in the presence of SED [Doherty et al., 2004; Liu et al., 2016a].

At 18:00–24:00 UT, the range of a zonal positive storm gradually depleted and disappeared, while a weak negative storm was observed at the high latitudes of the NH. It is most likely that under the effects of Joule heating and auroral electrojets, the neutral atmosphere expanded and rose, which may have brought N_2 molecules from the lower altitudes to higher altitudes and caused further decrease of the O/N_2 ratio. From 16:00 UT, a clear TEC enhancement can be seen below $20^\circ N$ in American sector. The most dramatic response of the positive storm occurred between $30^\circ S$ and $50^\circ S$, where there was an enhancement of more than 300% at 00:00–05:00 UT on 18 March. In contrast, we observed a negative storm in the corresponding region of the NH, which demonstrated an inverse hemispheric asymmetry in intensity and structure: a strong positive storm over South America and the South Atlantic, whereas a negative storm over North America.

From 06:00 to 12:00 UT on 18 March, a positive storm could be observed at low latitudes, which drifted westward and gradually decayed. While a clear negative storm occurred in the middle and high latitudes, which was especially apparent over East Asia and South Oceania (with a decrease of $\sim -100\%$). The negative storm emerged globally (except at certain low latitudes at 00:00–12:00 UT) on 18 March; this global negative storm became particularly apparent at 14:00–20:00 UT. On 19 March, because of the gradual return of solar and geomagnetic activities, the ionosphere slowly recovered to normal levels.

To study the temporal response of the ionospheric storm with respect to quiet days, the daily GIMs released by the International Global Navigation Satellite Systems Service (IGS)-Ionosphere working group are included in this study [Schaer, 1999; Hernández-Pajares et al., 2009]. We first take the GIM mean value for magnetic quiet days (11–15 March) as the reference value. Then, the RMS (16–22 March) with 2 h intervals can be calculated by using formula (6):

$$RMS_k = \sqrt{\frac{\sum_{i=1}^N (VTEC_i^k - VTEC_{ref,i}^k)^2}{N}} \quad k = 0, 2, 4, \dots, 22, 24 \quad (6)$$

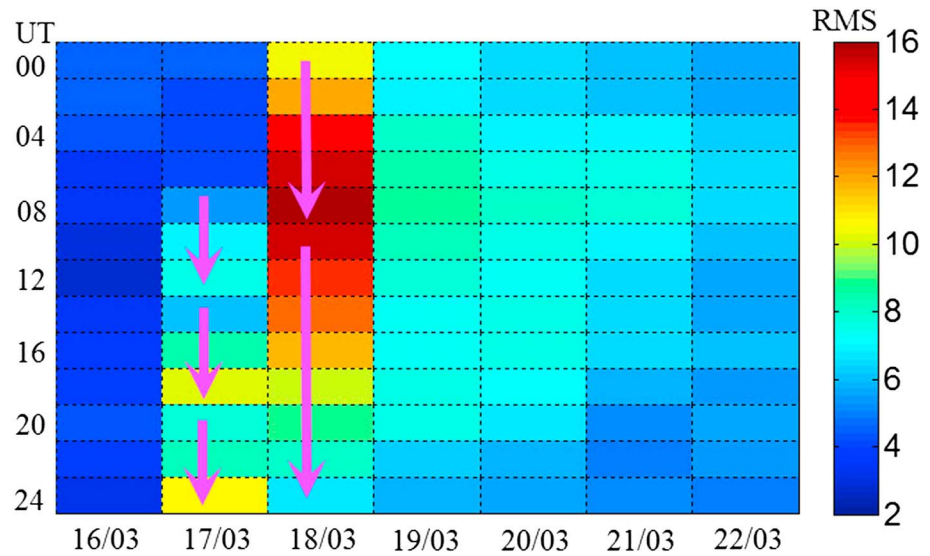


Figure 3. RMS from GIMs during 16–22 March 2015.

where RMS_k , reflecting the deviation from the quiet days, is the root-mean-square error at time k ; N is the grid number of an IONosphere Exchange (IONEX) map, which is equal to $71 \times 73 = 5183$; $VTEC_i^k$ and $VTEC_{ref,i}^k$ are, respectively, the observation and reference values at time k for grid number i .

As shown in Figure 3, the RMS for each period of the magnetic quiet day (16 March) is around 2–4, which can be regarded as the RMS of a calm state. The storm initiated at ~06:00 UT on 17 March and lasted for over 36 h. On 17 March, the RMS (marked by the purple arrow in Figure 3) changed 3 times from small to large (06:00–12:00 UT, 14:00–18:00 UT, and 20:00–24:00 UT); therefore, it is most likely that there were at least three global TIDs. We found that the three TIDs were consistent with the three-peak stages of *AE* (section 4.2 will focus on these three TIDs). On 18 March, the disturbances experienced a transition from weak (00:00 UT) to strong (08:00 UT), and then decayed again (24:00 UT). During 19–22 March, the ionosphere gradually returned to normal levels; however, a small-amplitude perturbation persisted, probably associated with ongoing auroral activities.

4.2. Three TIDs Observed in the Main Phase

One interesting topic that has been observed but not fully explored in section 4.1 is the three TIDs in the main phase. To further analyze the global propagation characteristics of these three TIDs, Figure 4 presents the global ROTI images of these three perturbation periods. The ROTI data were binned and averaged in cells of 2.5° latitude and 5° longitude with a sliding 10 min duration.

During the first disturbance period (06:00–10:00 UT), accompanied by significantly increased auroral activities (see *AE* index in Figure 1), the disturbances appeared at high latitudes of both hemispheres at ~07:00 UT and were particularly obvious in the high-latitude region of North America. From 07:00 to 09:00 UT, the TID gradually strengthened in amplitude and seemed to expand equatorward; this propagation of TID toward the equator was especially apparent in North America and the southern Australia sector. The maximum disturbance intensity occurred at ~09:00 UT (1 TECU/min), which was likely related to particularly strong auroral activities (the *AE* index at the first peak, at ~8:50 UT, was 981 nT). During 09:00–10:00 UT, the TID continued to propagate to low latitudes, while the amplitude faded somewhat.

During the second disturbance period (12:00–16:00 UT), the ROTI also responded acutely to ionospheric disturbances at high latitudes; it developed gradually from weak to strong, then weakened again in both hemispheres with the variation of the *AE* index. With the emergence of the *AE* peak (2046 nT, 13:55 UT), the ROTI reached a maximum value. We found that during ~14:00–16:00 UT, the equatorward TID was particularly apparent in the $\sim 95^\circ\text{E}$ – 180°E sector. Moreover, the amplitude and equatorward tendency of the TID in the NH were more notable than that in the SH, this again proved the hemispheric asymmetry of this ionospheric storm.

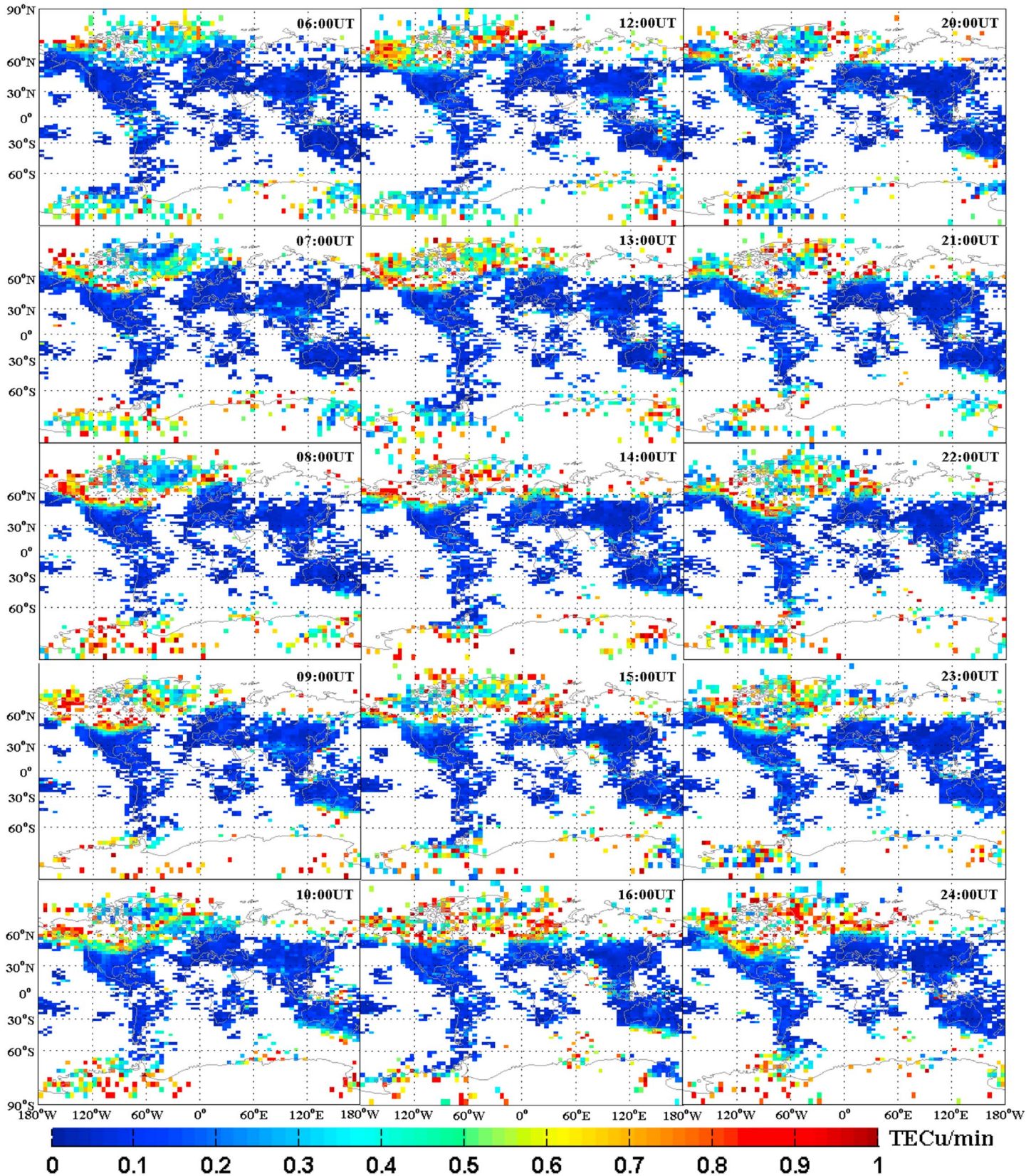


Figure 4. Hourly global ROTI of the three TIDs on 17 March (left column: 06:00–10:00 UT, middle column: 12:00–16:00 UT, right column: 20:00–24:00 UT).

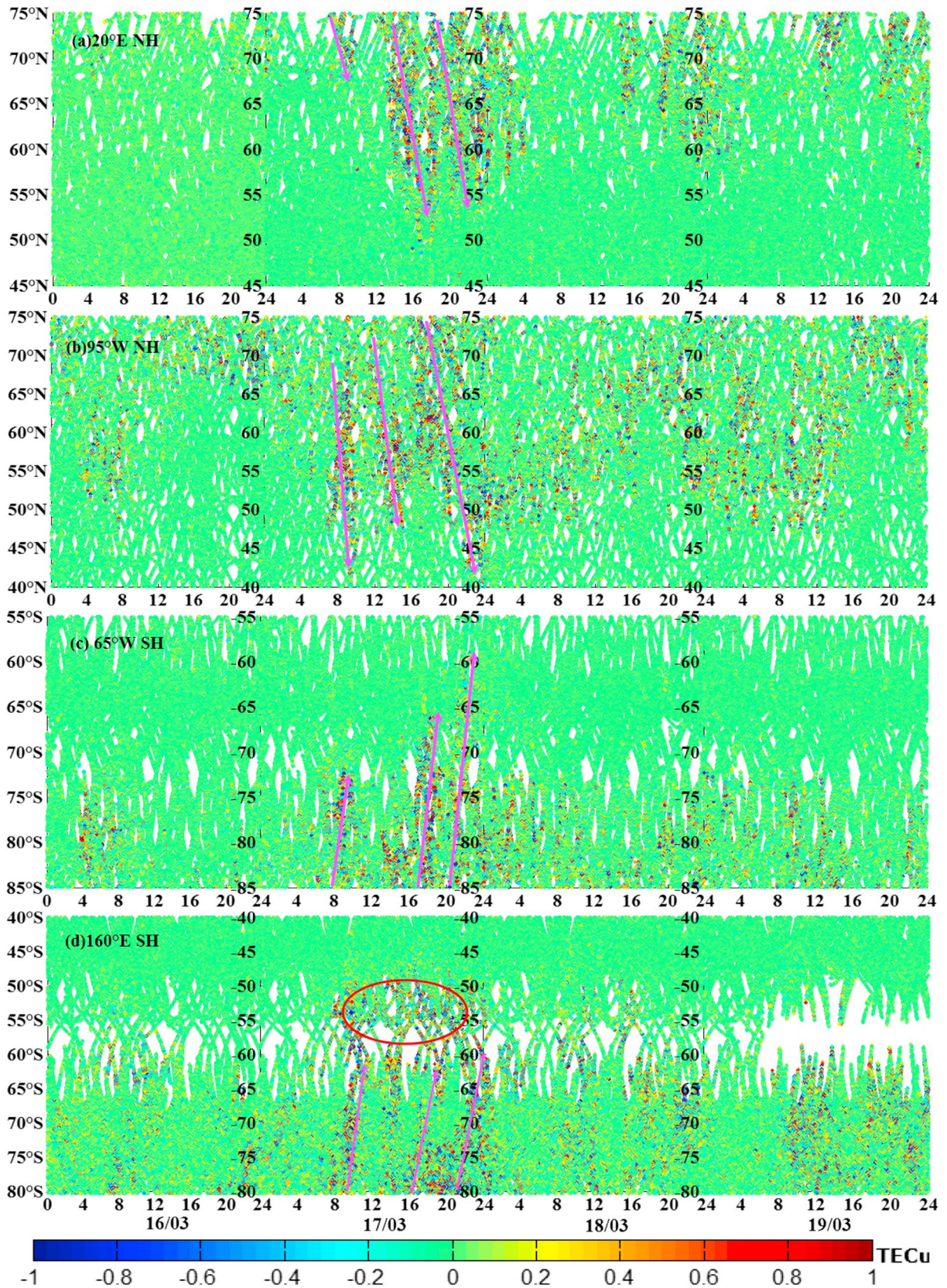


Figure 5. Variability of TECu perturbations over four different meridional chains (the horizontal axis shows the time in UT, and the vertical axis indicates the longitude of TECT): (a) 20°E NH, (b) 95°W NH, (c) 65°W SH, and (d) 160°E SH (NH and SH refer to Northern Hemisphere and Southern Hemisphere, respectively).

Table 1. Disturbance Periods of the Main Phase for Corresponding Indices in This Study

Corresponding Index	The First Disturbance Period	The Second Disturbance Period	The Third Disturbance Period
AE maximum	08:50 UT	13:55 UT	17:00–24:00 UT
SYM-H minimum	09:35 UT	17:25 UT	22:45 UT
GIM RMS	6:00–12:00 UT	14:00–18:00 UT	20:00–24:00 UT
Global ROTI	6:00–10:00 UT	12:00–16:00 UT	20:00–24:00 UT
TECT of chains	7:00–10:00 UT	13:00–18:00 UT	19:00–24:00 UT

During the third disturbance period (20:00–24:00 UT), auroral activities were particularly active. Therefore, the ROTI showed a clear trend toward the equator. In particular, the irregular disturbance zone expanded equatorward to $\sim 40^\circ\text{N}$ over North America ($\sim 24:00$ UT).

To represent the propagation of the three TIDs intuitively, we have also selected TECT of four north-south chains from different GPS stations for further analysis. Figure 5 shows the TECT fluctuations in the main phase and recovery phase. More importantly, three equatorward TIDs are found in the various chains, and each TID from different chains occurred almost simultaneously, with only slight differences in variables such as propagation distance and perturbation amplitude. The three disturbance periods ($\sim 7:00$ – $10:00$ UT, $13:00$ – $18:00$ UT, and $19:00$ – $24:00$ UT) not only correspond roughly to the three peak phases of AE but were also consistent in terms of RMS and ROTI (see Table 1).

During the first disturbance period, the propagation distance and perturbation range of each chain varied from the others. The TID at $95^\circ\text{W}_{\text{NH}}$ spread the farthest (nearly to 45°N), followed by that at $160^\circ\text{E}_{\text{SH}}$, the TID at $65^\circ\text{W}_{\text{SH}}$ traveled to 70°S , and the disturbance range at $20^\circ\text{E}_{\text{NH}}$ was the smallest. Our analysis revealed that the disturbance during the first disturbance period was likely related to auroral energetic particle precipitation (see AE index in Figure 1). During the second disturbance period, similar equatorward TIDs also occurred at different chains. The TID at $20^\circ\text{E}_{\text{NH}}$, which spread to as far as $\sim 50^\circ\text{N}$, was strongly apparent; meanwhile, the TID at $95^\circ\text{W}_{\text{SH}}$ changed from weak to strong again and then decayed until it disappeared. An intense TID at $65^\circ\text{W}_{\text{NH}}$ that propagated to low latitudes was easily observed, whereas the disturbance amplitude and range at $160^\circ\text{E}_{\text{SH}}$ were weaker than those of the other meridional chains evaluated. It is most likely that the TID during this period corresponded to the second peak phase of AE (2046 nT, 13:55 UT), suggesting that energy was continuously injected into the polar region. For the TID of the third period, we found that it overlapped with the TID of the second period, because the two TIDs traveled together to low latitudes. This interesting phenomenon was especially evident at $65^\circ\text{W}_{\text{NH}}$ and $95^\circ\text{W}_{\text{SH}}$. We concluded that because of the long-term southward B_z and the third AE peak of this period, this TID had the longest duration, the largest amplitude, and the relatively great propagation distance.

Because of the persistent auroral activity during 18–19 March, degrees of ionospheric disturbances at high latitudes varied across all chains. It should also be noted that an obvious westward displacement of disturbances was observed in the $\sim 45^\circ\text{S}$ – 60°S sector at a longitude of $160^\circ\text{W}_{\text{SH}}$ on 19 March, which can be explained by the effect of the Coriolis force and the westward thermospheric wind [Oliver *et al.*, 1997; Afraimovich *et al.*, 2000].

4.3. The Evolution of the Negative Storm in the Recovery Phase

As mentioned in section 4.1, the negative storm emerged globally in the recovery phase, which was especially apparent over East Asia and South Oceania; therefore, we take the ionosphere effects of f_oF_2 over East Asia as an example to further illustrate the evolution of the negative storm.

The variations of f_oF_2 recorded by ionosondes in China ($\sim 115^\circ\text{E}$) during 16–20 March 2015 were first used to illustrate the evolution of this storm (positive \rightarrow negative \rightarrow normal level). From Figure 6, one can notice that after 12:00 UT on 17 March, the f_oF_2 recorded from Mohe (52.9°N , 122.5°E), Beijing (40.3°N , 116.3°E), Wuhan (30.5°N , 114.3°E), and Sanya (18.3°N , 109°E) transitioned gradually from higher to lower than the reference value (positive storm \rightarrow negative storm), which indicated that the negative storm spread from high latitudes to low latitudes over the time. On 18 March, the f_oF_2 at different stations were far lower than the reference values by over 50%, suggesting that the negative storm response, which may be caused by the extremely low O/N₂ ratio, was significantly obvious. In recent studies of this storm, both Astafyeva *et al.* [2015] and Nayak *et al.* [2016] have also suggested that the composition change in the thermospheric neutral wind is

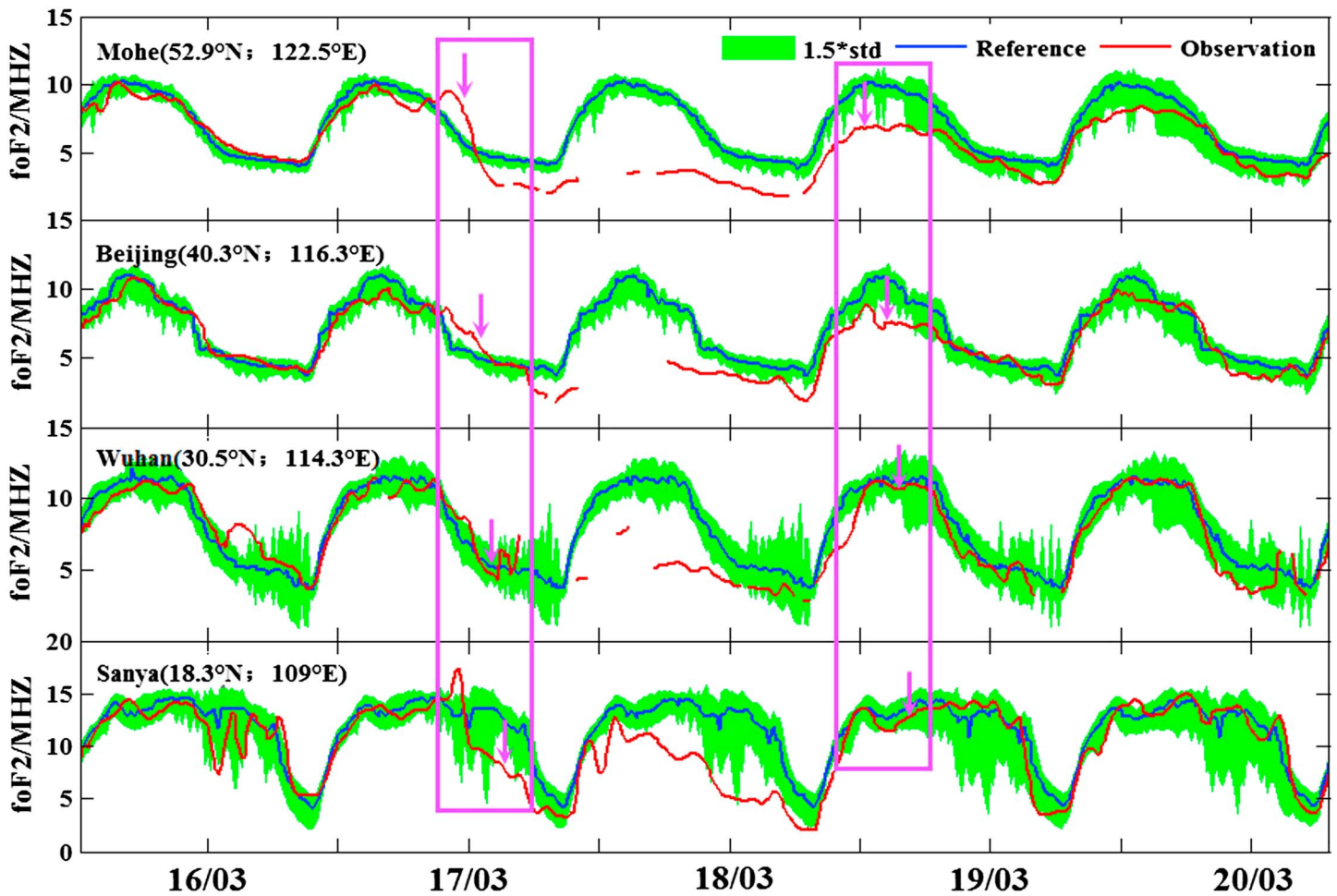


Figure 6. Variations of f_oF_2 observed in China during 16–20 March 2015 (variation of f_oF_2 with a time resolution of 15 min is indicated by the red line, variation of the 15 day sliding median f_oF_2 is indicated by the blue line, and the 1.5 sigma standard deviation is indicated by the green line, which represents the limit of the day-to-day variability).

an important driver of the strong negative ionospheric storm effects in the recovery phase. On 19–20 March, the f_oF_2 at each station gradually returned to normal levels from negative storm effects, which coincided with the variations of the differential VTEC maps (see Figure S2). Note that the most obvious decline of f_oF_2 was recorded at Mohe and Beijing stations, whereas the decrease at Sanya station was not as sharp, indicating that the intensity of the negative storm gradually decayed as it propagated to low latitudes. During the daytime of 19 March, a negative storm was clear in Mohe and then weakened in Beijing; finally, the ionosphere recovered to normal levels in Wuhan and Sanya; that means the negative storm decayed along with the propagation toward the equator, and the dominant physical mechanism related to the damping may be the ion-drag effect of the background ionosphere [Tsugawa *et al.*, 2003].

5. Discussions and Conclusions

The largest geomagnetic storm of solar cycle 24 thus far occurred in March 2015 and caused dramatic and complex ionospheric storm effects, which were dominated by various drivers and mechanisms at different phases.

1. Based on the differential VTEC maps in the spatial domain, the VTEC enhancement occurred preferentially in the high latitudes of the NH at 05:00 UT on 17 March, with a maximum increase of approximately 50% relative to mean VTEC, meaning that the energy was continuously injected into the polar region. In the following 7 h, the positive storm gradually strengthened (with a maximum increase of over 150%) and

expanded equatorward. *Nayak et al.* [2016] found a similar enhancement in $h_m F_2$ at all stations of the American sector during the first minimum of the *SYM-H*, and they proposed that this enhancement could be caused by the prompt penetration electric fields associated with fluctuating IMF B_z . From 12:00 UT to 15:00 UT, a weak negative storm (decrease of approximately -50% to -80%) was dominant in the high latitudes of the SH, whereas the increase in range and amplitude of the positive storm in the NH became less significant, and at this time, the *AE* index was in the low level, which indicated that the auroral activity level decreased. At 18:00–24:00 UT, a negative storm emerged in the high latitudes of the NH; it was most likely that under the effects of Joule heating and auroral electrojets, the neutral atmosphere expanded and transported N_2 molecules from the lower atmosphere to higher altitudes, and thus, the O/N_2 ratio decreased.

2. From the RMS of GIMs in the temporal domain, we found, for the first time, that there were at least three TIDs (06:00–12:00 UT, 14:00–18:00 UT, and 20:00–24:00 UT) in the main phase of this storm and that the disturbance periods and *AE* peak stages were roughly synchronous. Based on these findings, we also analyzed the propagation characteristics of the three TIDs from global ROTI and found that the TIDs were first observed at high latitudes (the amplitude somewhat faded when propagating to lower latitudes) and that the equatorward extension was particularly notable in North America (to $\sim 40^\circ N$, at $\sim 24:00$ UT). The three equatorward TIDs were also observed in the four selected meridional chains, and they were almost coincident with the three disturbance periods of the RMS and ROTI despite slight differences in propagation distance and perturbation amplitude due to latitudinal, longitudinal, and local time effects. We conclude that the three equatorward TIDs could be largely attributed to the AGWs which were excited by auroral substorm activities: the high-speed solar wind (> 500 km/s), accompanied by intensive southward IMF B_z , compressed the magnetic field, then the magnetosphere energy was transferred to the upper atmosphere of the high latitudes through Joule heating, Lorentz forces, or intense particle precipitations, etc. [*Hunsucker, 1982; Tsugawa et al., 2003, 2007*]. As a result, AGWs, interacting with the ionosphere, caused equatorward propagating TIDs and continuously delivered auroral energy to low-latitude regions.
3. From 16:00 UT, a clear TEC enhancement can be seen below $20^\circ N$ in American sector, along with the most dramatic response between $30^\circ S$ and $50^\circ S$ (over 300% enhancement at 00:00–05:00 UT on 18 March). In contrast, we observed a relatively weak negative storm at the corresponding region of the NH, finally forming the inverse hemispheric asymmetry in intensity and structure. Such hemispheric asymmetry is usually attributed to seasonal dependence (especially as the storm time thermosphere composition changes). Storm time circulation is imposed on the summer-to-winter background seasonal circulation, and as a result, positive storms generally commence in the winter hemisphere, while negative storms preferentially occur in the summer hemisphere [*Fuller-Rowell et al., 1994; Goncharenko et al., 2007; Daniilov, 2013*]. However, considering that this storm occurred only a few days before the spring equinox, the seasonal effects may not have played a leading role in generating this asymmetric structure.
 - a. In recent years, it has been found that the amplitude and direction of the IMF B_y component, which plays an important role in the development of ionospheric storms, may be one of the factors that impacts the hemispheric asymmetry [*Crowley et al., 2010; Förster et al., 2011; Mannucci et al., 2014; Astafyeva et al., 2015*]. In terms of the St. Patrick's Day storm, IMF B_y remained negative (southward) for a long time after 22:45 UT on 17 March, until the day on 18 March; consequently, we observed a sharp VTEC increase over South America and the Southern Atlantic Ocean.
 - b. Additionally, the geomagnetic field intensity may be another significant driver of the hemispheric asymmetry, because the positive storm was precisely located in the South Atlantic Anomaly (SAA) region, where the geomagnetic field intensity shows fairly negative magnetic properties (see Figure S3). Generally, affected by TIDs and equatorward neutral wind during storms, energetic electrons would reach and fill near the SAA region. However, the electrons did not drift past the SAA, but rather were trapped in it because of relatively weak geomagnetic constraints. Thereafter, they were brought to lower altitudes, eventually causing a sharp increase of VTEC in the SAA region [*Hartmann and Pacca, 2009; Lin and Yeh, 2005; Asikainen and Mursula, 2005*].
4. In the recovery phase (on 18 March), the negative storm of mid-high latitudes and the positive storm of low latitudes may be explained by the storm time circulation theory [*Fuller-Rowell et al., 1994; Fang et al., 2012*]: with the sudden enhancement of energetic particle precipitation and significantly increased auroral electrojets, the upper atmosphere was heated through Joule heating and Lorentz forces. The

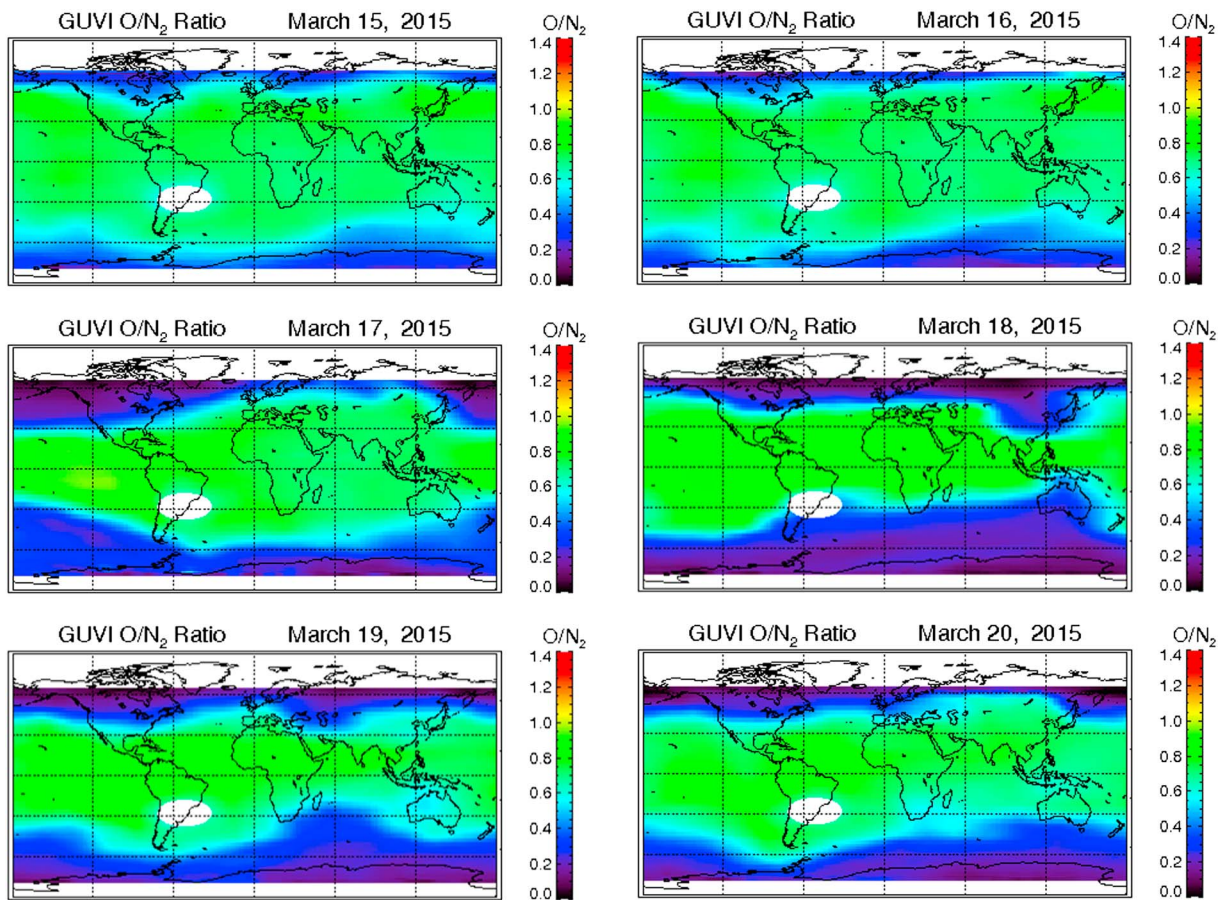


Figure 7. Maps showing the thermospheric O/N_2 ratio during 15–20 March 2015.

auroral neutral atmosphere then expanded and moved upward, carrying with it a large amount of high-latitude thermospheric neutral composition; thereafter, they flowed to the low-latitude area under the effects of the horizontal equatorward thermospheric wind, and finally sank in the equatorial region. Likewise, the neutral atmosphere was also present in the lower thermosphere, moving from the equator to the polar region, and thus, the large-scale circulation formed. However, with increasing altitude, the reduction percentage of O atom became significantly lower than that of the N_2 molecule, and as a result, the O atom removal of high latitudes from the upper thermosphere surpassed the supply from the lower thermosphere, which led to a considerable decrease of the thermospheric O/N_2 ratio in the auroral region. This decrease is why significant negative storms are observed at high latitudes. Additionally, the number of O atoms brought from the poles in the upper thermosphere was greater than the number carried from the equator to the poles in the lower thermosphere; consequently, as a result of the increased O/N_2 ratio, positive storms prevailed at low latitudes. Moreover, the thermospheric O/N_2 ratio maps over 15–20 March, derived from TIMED/GUVI (see Figure 7), provided evidence that the evolution of this negative storm was related to the storm circulation theory: it was found that the O/N_2 ratio at mid-high latitudes during 16–18 March remained depressed and that these low values seemed to expand equatorward. Accordingly, the middle and high latitudes of both hemispheres experienced an evolution from positive storms to negative storms, so did the f_oF_2 variations in China. We also observed that the O/N_2 ratio was lowest on 18 March, and the coverage was highest; therefore, the ionospheric storm around the globe, especially at middle and high latitudes, were mainly negative. In recent studies of this storm, both *Astafyeva et al.* [2015] and *Nayak et al.* [2016] have also suggested that the composition change in the thermospheric neutral wind is an important driver of the strong negative ionospheric storm effects in the recovery phase. Compared with the O/N_2 ratio on 18 March, the one during 19–20 March had been remarkably restored and gradually contracted to the polar region, which corresponded to the recovery

of the VTEC (negative storm \rightarrow normal level). It is worth noting that the significant decrease of the O/N_2 ratio was most pronounced over East Asia and Australia on 18 March, and the lower O/N_2 ratio reached the low latitudes of the Asian sector. Therefore, obvious negative storms were observed from the differential VTEC maps (see Figure S2), and the composition changes were in consistent with the evolution of f_oF_2 observed by the ionosondes in China (see Figure 6).

Acknowledgments

We thank the SOPAC (<http://sopac.ucsd.edu/sopacDescription.shtml>), EUREF (<ftp://rgpddata.ign.fr>), CACS (<http://www.nrcan.gc.ca/home>), CMONOC (<http://www.neiscn.org/>), and Geoscience Australia (<ftp://ftp.ga.gov.au>) for providing the GPS data. The authors are grateful to the IGS (<ftp://cddis.nasa.gov/pub/gps/products/ionex/>) for the IONEX products, the Johns Hopkins University Applied Physics Laboratory (<http://guitimed.jhuapl.edu>) for the thermospheric O/N_2 density maps, and the Center for Space Environment Research and Forecast in China (<http://www.cserf.ac.cn/>) for the ionosonde data. The authors are also grateful to the NASA/GSFC Space Physics Data Facility's OMNIWeb service (<http://omniweb.gsfc.nasa.gov>) for the interplanetary and *SYM-H* parameter data; the Jicamarca observatory (<http://jro.igp.gob.pe/database/>) for the planetary index *Kp* data; the World Data Center for Geomagnetism, Kyoto University (<http://wdc.kugi.kyoto-u.ac.jp>) for the *AE* data; and the National Centers For Environmental Information of NOAA (<http://www.nesdis.noaa.gov>) for the geomagnetic field intensity. This work was supported by the National Key Research and Development Program of China (2016YFB0501803), the National Natural Science Foundation of China (41274022 and 41574028), the National Science Foundation for Distinguished Young Scholars of Hubei Province of China (2015CFA036), and the National Science Foundation for Young Scientists of China (41604002).

References

- Aarons, J. (1997), Global Positioning System phase fluctuations at auroral latitudes, *J. Geophys. Res.*, *102*(A8), 17,219–17,231, doi:10.1029/97JA01118.
- Afraimovich, E. L., E. A. Kosogorov, L. A. Leonovich, K. S. Palamartchouk, N. P. Perevalova, and O. M. Pirog (2000), Observation of large-scale traveling ionospheric disturbances of auroral origin by global GPS networks, *Earth Planets Space*, *52*(10), 669–674, doi:10.1186/BF03352261.
- Asikainen, T., and K. Mursula (2005), Filling the South Atlantic anomaly by energetic electrons during a great magnetic storm, *Geophys. Res. Lett.*, *32*, L16102, doi:10.1029/2005GL023634.
- Astafyeva, E., Y. Yasyukevich, A. Maksikov, and I. Zhivetiev (2014), Geomagnetic storms, super-storms, and their impacts on GPS-based navigation systems, *Space Weather*, *12*, 508–525, doi:10.1002/2014SW001072.
- Astafyeva, E., I. Zakharenkova, and M. Förster (2015), Ionospheric response to the 2015 St. Patrick's Day storm: A global multi-instrumental overview, *J. Geophys. Res. Space Physics*, *120*, 9023–9037, doi:10.1002/2015JA021629.
- Blanc, M., and A. D. Richmond (1980), The ionospheric disturbance dynamo, *J. Geophys. Res.*, *85*(A4), 1669–1686, doi:10.1029/JA085iA04p01669.
- Buonsanto, M. J. (1999), Ionospheric storms—A review, *Space Sci. Rev.*, *88*(3–4), 563–601, doi:10.1023/A:1005107532631.
- Cherniak, I., I. Zakharenkova, and R. J. Redmon (2015), Dynamics of the high-latitude ionospheric irregularities during the 17 March 2015 St. Patrick's Day storm: Ground-based GPS measurements, *Space Weather*, *13*, 585–597, doi:10.1002/2015SW001237.
- Crowley, G., D. J. Knipp, K. A. Drake, J. Lei, E. Sutton, and H. Lühr (2010), Thermospheric density enhancements in the dayside cusp region during strong BY conditions, *Geophys. Res. Lett.*, *37*, L07110, doi:10.1029/2009GL042143.
- Danilov, A. D. (2013), Ionospheric F-region response to geomagnetic disturbances, *Adv. Space Res.*, *52*(3), 343–366, doi:10.1016/j.asr.2013.04.019.
- Ding, F., W. Wan, B. Ning, and M. Wang (2007), Large-scale traveling ionospheric disturbances observed by GPS total electron content during the magnetic storm of 29–30 October 2003, *J. Geophys. Res.*, *112*, A06309, doi:10.1029/2006JA012013.
- Doherty, P., A. J. Coster, and W. Murtagh (2004), Space weather effects of October–November 2003, *GPS Solut.*, *8*(4), 267–271, doi:10.1007/s10291-004-0109-3.
- Fang, H., L. Weng, and Z. Sheng (2012), Variations in the thermosphere and ionosphere response to the 17–20 April 2002 geomagnetic storms, *Adv. Space Res.*, *49*(49), 1529–1536, doi:10.1016/j.asr.2012.02.024.
- Farrugia, C. J., V. K. Jordanova, M. F. Thomsen, G. Lu, S. W. H. Cowley, and K. W. Ogilvie (2006), A two-ejecta event associated with a two-step geomagnetic storm, *J. Geophys. Res.*, *111*, A11104, doi:10.1029/2006JA011893.
- Förster, M., S. E. Haaland, and E. Doornbos (2011), Thermospheric vorticity at high geomagnetic latitudes from CHAMP data and its IMF dependence, *Ann. Geophys.*, *29*(1), 181–186.
- Fuller-Rowell, T. J., M. V. Codrescu, R. J. Moffett, and S. Quegan (1994), Response of the thermosphere and ionosphere to geomagnetic storms, *J. Geophys. Res.*, *99*(A3), 3893–3914, doi:10.1029/93JA02015.
- Goncharenko, L. P., J. C. Foster, A. J. Coster, C. Huang, N. Aponte, and L. J. Paxton (2007), Observations of a positive storm phase on September 10, 2005, *J. Atmos. Sol. Terr. Phys.*, *69*(10), 1253–1272, doi:10.1016/j.jastp.2006.09.011.
- Hartmann, G. A., and I. G. Pacca (2009), Time evolution of the South Atlantic magnetic anomaly, *Anais da Acad. Brasileira de Ciências*, *81*(2), 243–255, doi:10.1590/S0001-37652009000200010.
- Hernández-Pajares, M., J. M. Juan, J. Sanz, R. Orus, A. Garcia-Rigo, J. Feltens, A. Komjathy, S. C. Schaer, and A. Krankowski (2009), The IGS VTEC maps: A reliable source of ionospheric information since 1998, *J. Geod.*, *83*(3–4), 263–275, doi:10.1007/s00190-008-0266-1.
- Huang, C. S., J. C. Foster, L. P. Goncharenko, P. J. Erickson, W. Rideout, and A. J. Coster (2005), A strong positive phase of ionospheric storms observed by the Millstone Hill incoherent scatter radar and global GPS network, *J. Geophys. Res.*, *110*, A06303, doi:10.1029/2004JA010865.
- Hunsucker, R. D. (1982), Atmospheric gravity waves generated in the high-latitude ionosphere: A review, *Rev. Geophys.*, *20*(2), 293–315, doi:10.1029/RG020i002p00293.
- Kamide, Y., and K. Kusano (2015), No major solar flares but the largest geomagnetic storm in the present solar cycle, *Space Weather*, *13*, 365–367, doi:10.1002/2015SW001213.
- Kamide, Y., N. Yokoyama, W. Gonzalez, B. T. Tsurutani, I. A. Daglis, A. Brekke, and S. Masuda (1998), Two-step development of geomagnetic storms, *J. Geophys. Res.*, *103*(A4), 6917–6921, doi:10.1029/97JA03337.
- Kappenman, J. G. (1996), Geomagnetic storms and their impact on power systems, *IEEE Power Eng. Rev.*, pp. 5–8, May.
- Kikuchi, T., K. K. Hashimoto, and K. Nozaki (2008), Penetration of magnetospheric electric fields to the equator during a geomagnetic storm, *J. Geophys. Res.*, *113*, A06214, doi:10.1029/2007JA012628.
- Kozyra, J. U., M. W. Liemohn, C. R. Clauer, A. J. Ridley, M. F. Thomsen, J. E. Borovsky, J. L. Roeder, V. K. Jordanova, W. D. Gonzalez (2002), Multistep Dst development and ring current composition changes during the 4–6 June 1991 magnetic storm, *J. Geophys. Res.*, *107*(A8)1224, doi:10.1029/2001JA000023.
- Lemaire, J. F., and K. I. Gringauz (1998), *The Earth's Plasmasphere*, *Earths Plasmasphere*, Cambridge Univ. Press, New York.
- Lin, C. S., and H. C. Yeh (2005), Satellite observations of electric fields in the South Atlantic anomaly region during the July 2000 magnetic storm, *J. Geophys. Res.*, *110*, A03305, doi:10.1029/2003JA010215.
- Liu, J., W. Wang, A. Burns, X. Yue, S. Zhang, Y. Zhang, and C. Huang (2016a), Profiles of ionospheric storm-enhanced density during the 17 March 2015 great storm, *J. Geophys. Res. Space Physics*, *121*, 727–744, doi:10.1002/2015JA021832.
- Liu, J., W. Wang, A. Burns, S. C. Solomon, S. Zhang, Y. Zhang, and C. Huang (2016b), Relative importance of horizontal and vertical transports to the formation of ionospheric storm-enhanced density and polar tongue of ionization, *J. Geophys. Res. Space Physics*, *121*, 8121–8133, doi:10.1002/2016JA022882.
- Mannucci, A. J., B. T. Tsurutani, M. A. Abdu, W. D. Gonzalez, A. Komjathy, E. Echer, B. A. Iijima, G. Crowley, and D. Anderson (2008), Superposed epoch analysis of the dayside ionospheric response to four intense geomagnetic storms, *J. Geophys. Res.*, *113*, A00A02, doi:10.1029/2007JA012732.

- Mannucci, A. J., G. Crowley, B. T. Tsurutani, O. P. Verkhoglyadova, A. Komjathy, and P. Stephens (2014), Interplanetary magnetic field BY control of prompt total electron content increases during superstorms, *J. Atmos. Sol. Terr. Phys.*, *115*, 7–16, doi:10.1016/j.jastp.2014.01.001.
- Maruyama, N., A. D. Richmond, T. J. Fuller-Rowell, M. V. Codrescu, S. Sazykin, F. R. Toffoletto, R. W. Spiro, and G. H. Millward (2005), Interaction between direct penetration and disturbance dynamo electric fields in the storm-time equatorial ionosphere, *Geophys. Res. Lett.*, *32*, L17105, doi:10.1029/2005GL023763.
- Nayak, C., L. C. Tsai, S. Y. Su, I. A. Galkin, A. T. K. Tan, E. Nofri, and P. Jamjareeulgarn (2016), Peculiar features of the low-latitude and midlatitude ionospheric response to the St. Patrick's Day geomagnetic storm of 17 March 2015, *J. Geophys. Res. Space Physics*, *121*, 7941–7960, doi:10.1002/2016JA022489.
- Oliver, W. L., Y. Otsuka, M. Sato, T. Takami, and S. Fukao (1997), A climatology of F region gravity wave propagation over the middle and upper atmosphere radar, *J. Geophys. Res.*, *102*(A7), 14,499–14,512, doi:10.1029/97JA00491.
- Pi, X., A. J. Mannucci, U. J. Lindqwister, and C. M. Ho (1997), Monitoring of global ionospheric irregularities using the worldwide GPS network, *Geophys. Res. Lett.*, *24*(18), 2283–2286, doi:10.1029/97GL02273.
- Rideout, W., and A. Coster (2006), Automated GPS processing for global total electron content data, *GPS Solut.*, *10*(3), 219–228, doi:10.1007/s10291-006-0029-5.
- Rishbeth, H., and M. Mendillo (2001), Patterns of F2-layer variability, *J. Atmos. Sol. Terr. Phys.*, *63*(15), 1661–1680, doi:10.1016/S1364-6826(01)00036-0.
- Rishbeth, H., and C. Setty (1961), The F-layer at sunrise, *J. Atmos. Terr. Phys.*, *20*(4), 263–276, doi:10.1016/0021-9169(61)90205-7.
- Saito, A., S. Fukao, and S. Miyazaki (1998), High resolution mapping of TEC perturbations with the GSI GPS network over Japan, *Geophys. Res. Lett.*, *25*(16), 3079–3082, doi:10.1029/98GL52361.
- Schaer, S. (1999), Mapping and predicting the Earth's ionosphere using the global positioning system, PhD thesis, 208 pp., Astron. Inst. of the Univ. of Bern, Switzerland.
- Scherliess, L., and B. G. Fejer (1997), Storm-time dependence of equatorial disturbance dynamo zonalelectric fields, *J. Geophys. Res.*, *102*(A11), 24,037–24,046, doi:10.1029/97JA02165.
- Schunk, R. W., and A. F. Nagy (2000), *Ionospheres: Physics, Plasma Physics, and Chemistry*, Cambridge Univ. Press, New York.
- Skone, S., and R. Yousuf (2007), Performance of satellite-based navigation for marine users during ionospheric disturbances, *Space Weather*, *5*, S01006, doi:10.1029/2006SW000246.
- Tsugawa T., A. Saito, Y. Otsuka, and M. Yamamoto (2003), Damping of large-scale traveling ionospheric disturbances detected with GPS networks during the geomagnetic storm, *J. Geophys. Res.*, *108*(A3), 1127, doi:10.1029/2002JA009433.
- Tsugawa, T., Y. Otsuka, A. J. Coster, and A. Saito (2007), Medium-scale traveling ionospheric disturbances detected with dense and wide TEC maps over North America, *Geophys. Res. Lett.*, *34*, L22101, doi:10.1029/2007GL031663.
- Tsurutani, B., et al. (2004), Global dayside ionospheric uplift and enhancement associated with interplanetary electric fields, *J. Geophys. Res.*, *109*, A08302, doi:10.1029/2003JA010342.
- Zhao, B., W. Wan, L. Liu, K. Igarashi, K. Yumoto, and B. Ning (2009), Ionospheric response to the geomagnetic storm on 13–17 April 2006 in the West Pacific region, *J. Atmos. Sol. Terr. Phys.*, *71*(1), 88–100, doi:10.1016/j.jastp.2008.09.029.
- Zhong, J., W. Wang, X. Yue, A. G. Burns, X. Dou, and J. Lei (2016), Long-duration depletion in the topside ionospheric total electron content during the recovery phase of the March 2015 strong storm, *J. Geophys. Res. Space Physics*, *121*, 4733–4747, doi:10.1002/2016JA022469.
- Zhu, Z. P., B. Q. Ning, W. X. Wan, B.-Q. Zhao, and M. Wang (2007), An investigation of ionospheric responses during the magnetic storm of 13–17 April 2006 at Western Pacific area, *Chin. J. Geophys.*, *50*(4), 824–836, doi:10.1002/cjg2.1100.